Spin–orbit photonic diode from biomimetic 3D chiral liquid crystal architectures

Gonzague Agez, Etienne Brasselet

OPTICA

Spin–orbit photonic diode from biomimetic 3D chiral liquid crystal architectures

Gonzague Agez[1,3] and Etienne Brasselet[2,4]

[1]CEMES, Université de Toulouse, CNRS, Toulouse, France
[2]Université de Bordeaux, CNRS, LOMA, UMR 5798, Talence, France
[3]e-mail: gonzague.agez@cemes.fr
[4]e-mail: etienne.brasselet@u-bordeaux.fr

Received 8 December 2021; revised 31 January 2022; accepted 5 February 2022; published 15 June 2022

Spin–orbit photonic devices usually rely on 2D (transverse) material structuring and are designed for optimal coupling between the polarization state and the spatial degrees of freedom at a given wavelength. Exploiting the third dimension (longitudinal) provides ways to bypass monochromatic limitations. Within a singular optics framework, here we show that chiral liquid crystals endowed with non-singular 3D helix axis orientational distribution exhibit transmissive broadband spin–orbit optical vortex generation as well as an optical diode effect. These results are in stark contrast to the properties of spin–orbit optical elements fabricated from chiral liquid crystals with a uniform orientation of the helix axis, which are reflective devices that process forward and backward propagating waves equally. Moreover, the similarities between the proposed 3D chiral structure and that of the cuticle of some insects invites considering spin–orbit photonics from a biological perspective.

https://doi.org/10.1364/OPTICA.450832

In the past two decades, substantial efforts have been made to develop strategies that enable light field structuring via geometrical principles. A prototypical situation relies on the use of the geometric phase, which is intimately rooted in the optical spin–orbit interaction, whenever the polarization state of light and the spatial degrees of freedom mutually interact. As such a beam shaping approach basically relies on the structure of the material rather than on its nature, it is particularly suitable for processing polychromatic light fields and a lot of classical and quantum outcomes have been identified; see, for instance, a recent set of reviews dealing with spin–orbit photonics [1–3]. In particular, the optical anisotropic properties of liquid crystalline mesophases and nowadays mature liquid crystal patterning technologies make it possible to fabricate high-resolution 2D flat-optics with arbitrary beam shaping functionalities that can be tunable and/or rewritable [4–6]. Noteworthy, the nano/microfabrication technologies that play a central role in spin–orbit photonics advances are mainly dealing with 2D designs and moving to 3D is expected to open up new perspectives. One example is the overcoming of inherently monochromatic designs of transmissive optical elements made from space-varying half-wave plates having inhomogeneous transverse distribution of the optical axis. Indeed, adding a continuous [7] or discrete [8] longitudinally varying contribution allows achieving enhanced chromatic performances. In particular, achromatic reflective optimal designs can be formally obtained when the longitudinal structuring of the optical axis is helical [9] and they have been identified to be of a spin–orbit nature [10,11]. The latter achromatic feature basically expresses in the spectral region associated with the circular photonic bandgap of chiral liquid crystals, which can be made as large as a few hundreds of nanometers in the visible domain by implementing strategies mimicking those found in living matter [12]. Still, to date, spin–orbit optical elements fabricated from chiral liquid crystals are designed to structure light beams from reflective designs endowed with uniform (1D) orientation of the helix axis.

By using a synthetic so-called polygonal texture [13] recalling that of the cuticle of some beetles [14]; see Fig. 1(a). Here we show that 3D helical architectures open up new spin–orbit photonic functionalities such as transmissive vortex beam shaping and an optical diode effect. Moreover, in the context of optical vortex generation, the present non-singular material structuring contrasts with the usual approach requiring singular structuring [15,16]. We use left-handed oligomers (Wacker Chemie GmbH) whose cholesteric (i.e., chiral nematic) mesophase exists in the temperature range 50°C–200°C, below which the material undergoes a glass transition, thus allowing us to scrutinize the frozen 3D internal liquid crystal structure at room temperature. The sample preparation follows the recipe detailed in [17], which consists of coating a $L \sim 13$ μm thick film of the compound kept at 140°C onto a bare glass substrate that defines the (x, y) plane. As the glass/medium and medium/air interfaces promote incompatible orientational boundary conditions (parallel and perpendicular, respectively), an irregular polygonal pattern develops. Each cell of this pattern is endowed with a smooth 3D chiral architecture, and from now on we focus on a single cell whose structural features are similar whatever the cell.

On the one hand, its effective transverse space-variant optical anisotropy is retrieved by polarimetric analysis (Abrio imaging system); see Fig. 1(b), showing an azimuthal distribution of the optical axis associated with a ring-shaped birefringence profile. On the other hand, the spin-dependent reflective spectral band in the typical range 550–700 nm (see later Fig. 4) is a characteristic

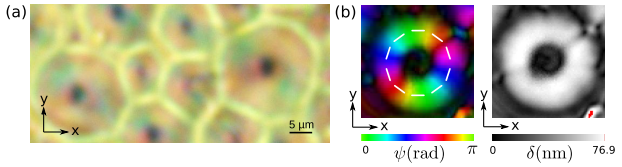

Fig. 1. (a) Bright field transmission optical image of the free surface of a so-called polygonal texture of a chiral liquid crystal. (b) Maps of the slow axis in-plane orientation angle ψ and anisotropic retardance magnitude δ of a polygonal cell.

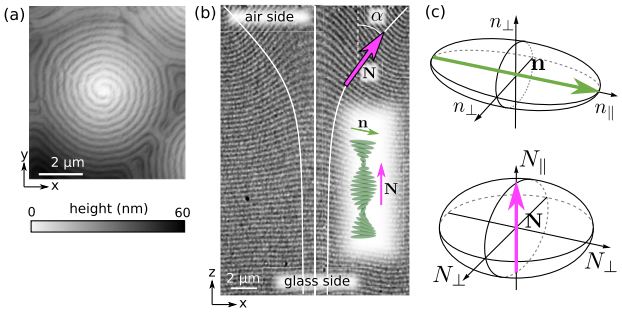

Fig. 2. (a) AFM top view and (b) TEM meridional view of a polygonal cell. (c) Ellipsoids of indices associated with the director field **n** and the helical field **N**; see text for details.

spectral signature of the helical order. Its direct spatial signature is obtained from an atomic force microscope (AFM) top view and transmission electron microscopy (TEM) meridional view; see Figs. 2(a) and 2(b). Indeed, as previously introduced in Ref. [18], the contrast of the images reveals the local orientation of the director n (i.e., the unit vector that defines the local average molecular orientation, noting the equivalence $\mathbf{n} \equiv -\mathbf{n}$). The distance between two bright lines corresponds to a π rotation of the director around the cholesteric helix axis denoted by the unit vector **N** (which satisfies $\mathbf{N} \equiv -\mathbf{N}$). The 3D character of the chiral director field is highlighted in Fig. 2, where the thin white lines refer to streamlines for the helical field **N**. With the aim at simulating the spin-dependent optical properties of the actual 3D optically anisotropic structure, and, neglecting the less than 100 nm height conical-shaped topography at the medium/air interface, hereafter we propose an analytical description of the 3D director field. We thus go beyond previous 2D optical simulations reported in [14], which discarded both the effects of the material birefringence and that of the polarization state of light.

The optical properties are locally defined by the uniaxial dielectric relative permittivity second-order tensor $\overline{\varepsilon}$. For a locally uniaxial liquid crystal as is the case here, it is defined by two principal values $\varepsilon_\perp = n_\perp^2$ and $\varepsilon_\parallel = n_\parallel^2$ that are related to the refractive indices perpendicular ($n_\perp$) and parallel ($n_\parallel$) to the director, respectively; see Fig. 2(c). Its expression in the coordinate system (x, y, z) is derived accounting for the knowledge inferred by the TEM structural characterization. At a given point **r**, the tensor $\overline{\varepsilon}$ is that of a helical director structure defined by two angles: the tilt angle $\alpha(\mathbf{r})$ of the helix vector **N** with respect to the z axis and the rotation angle $\chi(\mathbf{r})$ of the director around **N**. Choosing $\mathbf{n}_0 = (0, 1, 0)$ as the boundary condition at the glass/medium interface located at $z = 0$, the expression of $\overline{\varepsilon}$ is obtained by applying the composition of two rotations to the diagonal tensor $\overline{\varepsilon}_0 = \mathrm{diag}(\varepsilon_\perp, \varepsilon_\parallel, \varepsilon_\perp)$. Namely, a rotation by an angle χ around the z axis followed by a rotation by an angle α around the axis defined by the unit vector $\mathbf{\Phi} = (-\sin\phi, \cos\phi, 0)$, where ϕ is the usual polar angle in the (x, y) plane. From tensorial calculus one thus gets $\overline{\varepsilon} = R\overline{\varepsilon}_0 R^{\mathrm{T}}$, where $(\cdot)^{\mathrm{T}}$ refers to the transpose operation and $R = R_{\mathbf{\Phi}}(\alpha) R_{\mathbf{z}}(\chi)$ is the total rotation matrix associated to the above composition of two successive rotations. Using Rodrigues's rotation formula, we get

$$R_{\mathbf{z}}(\chi) = \begin{bmatrix} c_\chi & -s_\chi & 0 \\ s_\chi & c_\chi & 0 \\ 0 & 0 & 1 \end{bmatrix}, \tag{1}$$

$$R_{\mathbf{\Phi}}(\alpha) = \begin{bmatrix} s_\phi^2(1-c_\alpha)+c_\alpha & -s_\phi c_\phi(1-c_\alpha) & c_\phi s_\alpha \\ -s_\phi c_\phi(1-c_\alpha) & c_\phi^2(1-c_\alpha)+c_\alpha & s_\phi s_\alpha \\ -c_\phi s_\alpha & -s_\phi s_\alpha & c_\alpha \end{bmatrix}, \tag{2}$$

where $c_X = \cos X$ and $s_X = \sin X$ with $X = (\chi, \phi, \alpha)$. The nine terms of the local dielectric tensor in the (x, y, z) reference are thus calculated from the expression

$$\begin{bmatrix} \varepsilon_{xx} & \varepsilon_{xy} & \varepsilon_{xz} \\ \varepsilon_{yx} & \varepsilon_{yy} & \varepsilon_{yz} \\ \varepsilon_{zx} & \varepsilon_{zy} & \varepsilon_{zz} \end{bmatrix} = R_{\mathbf{\Phi}}(\alpha) R_{\mathbf{z}}(\chi) \begin{bmatrix} \varepsilon_\perp & 0 & 0 \\ 0 & \varepsilon_\parallel & 0 \\ 0 & 0 & \varepsilon_\perp \end{bmatrix} R_{\mathbf{z}}(-\chi) R_{\mathbf{\Phi}}(-\alpha). \tag{3}$$

The final step of the model consists in digitizing the angles $\alpha(\mathbf{r})$ and $\chi(\mathbf{r})$ from local 2D Fourier transform of the TEM image in the (x, z) plane shown in Fig. 2(b) multiplied by a binary amplitude mask with $1 \times 1\ \mu\mathrm{m}^2$ area. Indeed, **N** is locally collinear to the wavevector of the modulation, from which $\alpha_{\mathrm{exp}}(x, 0, z)$ is retrieved, while $\chi_{\mathrm{exp}}(x, 0, z)$ is retrieved as the phase associated to this wavevector. Then, assuming axisymmetric angle distributions around the z axis, one gets the whole 3D distribution for α and χ. The spatial distributions of the six independent components of the emulated dielectric tensor ($\varepsilon_{xy} = \varepsilon_{yx}$, $\varepsilon_{xz} = \varepsilon_{zx}$, $\varepsilon_{yz} = \varepsilon_{zy}$) are illustrated in Fig. 3. Then, the optical behavior of a polygonal cell can be simulated with the finite-difference time-domain (FDTD) method [19], using an open-source software package [20]. The computational box dimensions is $10 \times 10 \times 21\ \mu\mathrm{m}^3$ with a resolution of 20 nm. At each grid point, the dielectric tensor is defined according to Eq. (3) and using $n_\perp = 1.5$ and $n_\parallel = 1.7$.

First, we consider forward propagation for normally incident light that propagates toward $z > 0$ by launching a Gaussian beam

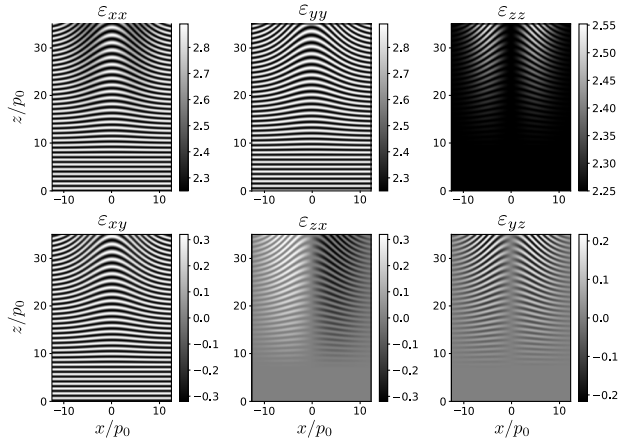

Fig. 3. Six independent components of $\overline{\varepsilon}$ emulated from the experimental TEM structural analysis in the plane (x, z). Note that the helical director pitch $p_0 = 2\pi/(d\chi/dz)_{z=0}$ at $z = 0$ and the sample thickness are chosen to ease the readability.

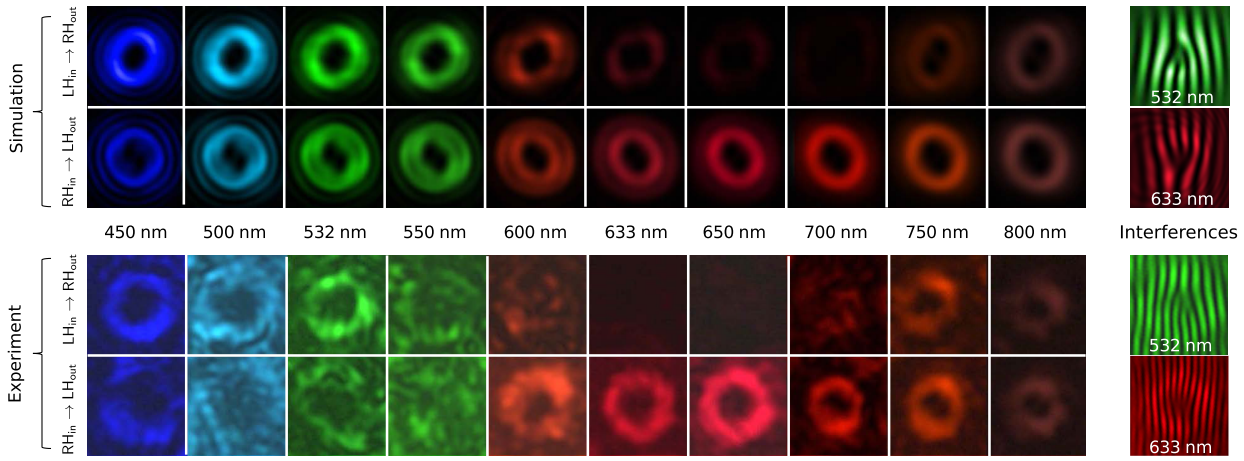

Fig. 4. Crossed circular polarized transmitted intensity distributions in the visible domain for left-handed (LH) and right-handed (RH) incident circular polarization states, for $\mathbf{k}_{in} \cdot \mathbf{z} > 0$, where $\mathbf{k}_{in}$ refers to the wavevector of the incident light beam. Rightmost part of the figure: interference intensity patterns obtained by superimposing an obliquely propagating reference beam onto the transmitted field at wavelength $\lambda = 532$ nm and $\lambda = 633$ nm, which demonstrate optical vortex generation with spin-dependent topological charge ± 2. Top: simulation. Bottom: experiment. Identical brightness scale is used for the two panels, for each wavelength.

with 5 μm waist radius at a distance 2 μm before it reaches the sample at $z = 0$ from an isotropic non-absorbing dielectric external medium with refractive index $n_{ext} = 1.6$. The results are displayed in the upper part of Fig. 4, which shows the spectral dependence of the crossed circular polarized output beam in the visible domain for left-handed (LH) and right-handed (RH) incident circular polarization states. It is noteworthy that spin-dependent optical vortex generation is predicted whatever the wavelength, though with vanishing efficiency for the LH incident circular polarization state for wavelengths belonging to the circular photonic bandgap of the helical director structure [Fig. 1(c)]. The vortex structure is identified by retrieving the singular phase spatial distribution of the circularly polarized components of the output field. This is illustrated here in the rightmost part of Fig. 4, which exhibits a fork-like interference intensity patterns with two teeth obtained from the coherent superposition of a reference beam with the output beam for both $LH_{in} \rightarrow RH_{out}$ and $RH_{in} \rightarrow LH_{out}$ processes at wavelength $\lambda = 532$ nm and $\lambda = 633$ nm, respectively. The up and down nature of the fork patterns demonstrate the production of optical vortices with spin-controlled topological charge ± 2.

In order to explain these observations, let us recall that a cholesteric liquid crystal having a uniform helical axis aligned along the propagation direction [i.e., $\alpha(\mathbf{r}) = 0$] merely behaves as a spin-dependent reflector even for nonuniform helical pitch (i.e., $d\chi/dz \neq 0$). This allows us to ascribe the spin-dependent optical vortex generation in the forward direction to the 3D axisymmetric distribution of the helical field $\mathbf{N}$. An intuitive understanding can be grasped by recalling the apparent negative optical anisotropy of cholesterics, as early noticed by Friedel [21]. Indeed, in the limit of large wavelength compared to the helical pitch, the effective ellipsoid of indices of a cholesteric is that of a negative uniaxial medium having a slow axis oriented along $\mathbf{N}$, as shown in Fig. 1(d), where $N_{\parallel} = n_{\perp}$ and $N_{\perp} = \frac{1}{2}(n_{\perp}^2 + n_{\parallel}^2)^{1/2}$. In addition, the non-singular 3D axisymmetric distribution of $\mathbf{N}$ is analog to director field $\mathbf{n}$ of a so-called umbilic defect of nonchiral nematics, which are known to behave as spin–orbit singular optical phase mask with topological charge ± 2 [22]. Qualitatively, we thus deal here with a hybrid non-singular spin–orbit optical vortex generator endowed with spectral discrimination features for the incident circular polarization state.

The above predicted spectrally sensitive transmissive spin–orbit vortex generation is observed by using the same set of wavelength values as summarized in the bottom part of Fig. 4. The crossed circular polarized transmission patterns are obtained by illuminating the sample with a ∼2 mm diameter collimated supercontinuum laser beam filtered with a set of bandpass filters with 10 nm full width half-maximum bandwidth. A polygonal cell is imaged using a 10× microscope objective with a 0.25 numerical aperture, and the input (output) circular polarization state is prepared (selected) by placing a linear polarizer followed by an electrically controlled liquid crystal variable retarder adjusted to operate as a quarter-wave plate for the considered wavelength before (after) the sample. These results agree fairly well with the numerical simulations. We note that additional laser sources having larger temporal coherence length than that of the supercontinuum light are used in order to ease the observation of interference patterns at $\lambda = 532$ nm and $\lambda = 633$ nm.

Second, we unveil a spin–orbit optical diode effect whose vivid occurrence is reported here at a wavelength that corresponds to the circular photonic bandgap experienced by an incident light that propagates toward $z > 0$. In that case, a left-handed incident circular polarization lead to virtually null transmission and null polarization conversion. This is shown in the upper part of Fig. 5 that displays the simulated polarization-resolved propagation of light through the polygonal cell for $\mathbf{k}_{in} \cdot \mathbf{z} > 0$ and $\lambda = 633$ nm. The experimental observation of null transmission supports the numerical results. In contrast, a LH circularly polarized beam undergoes polarization conversion, polarization selective transmission, and transmissive spin–orbit optical vortex generation for $\mathbf{k}_{in} \cdot \mathbf{z} < 0$, as numerically demonstrated in the bottom part of Fig. 5. Experimentally, the recorded total intensity pattern is found to be fully RH circularly polarized and corresponds to an optical vortex field, which also supports the numerical findings. These results highlight two main features of the polygonal cell structure. On the one hand, its helical structure is endowed with a spatially varying pitch as shown in Fig. 2(b). This implies that

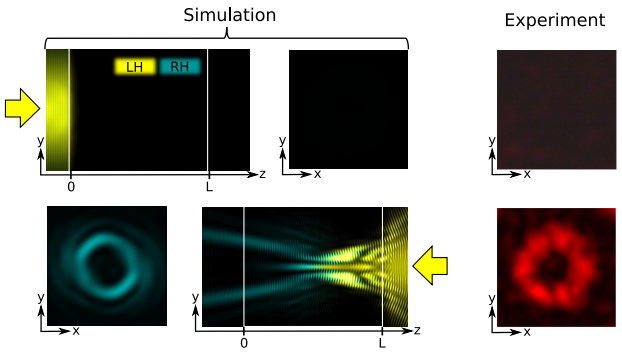

Fig. 5. Numerical simulations of the polarization-resolved propagation of light at $\lambda = 633$ nm for $\mathbf{k}_{in} \cdot \mathbf{z} > 0$ (top row) for $\mathbf{k}_{in} \cdot \mathbf{z} < 0$ (bottom row) at 633 nm wavelength. The yellow and cyan 8-bit color coding refer to LH and RH circularly polarized components, and the brightness refers to optical intensity. In each case, the experimental total output intensity pattern is shown, and the output polarization state of the optical vortex field for $\mathbf{k}_{in} \cdot \mathbf{z} < 0$ is found to be purely RH circularly polarized. In all simulation panels the cyan value is multiplied by five for better visual rendering.

the spin-dependent photonic bandgap associated with the local on-axis cholesteric structure near each of the two facets is different. This explains why the LH incident light is immediately reflected when $\mathbf{k}_{in} \cdot \mathbf{z} > 0$, while it can propagate in the bulk of the sample when $\mathbf{k}_{in} \cdot \mathbf{z} < 0$. On the other hand, the 3D character of the helical architecture ($\alpha \neq 0$) acts as an axisymmetric space-variant optically anisotropic retarder, which leads to polarization conversion and vortex beam shaping. Importantly, the converted RH component is immune to the spin-dependent photonic bandgap everywhere since the medium is LH. The RH component thus propagates through the polygonal cell and is eventually transmitted, while the unconverted fraction of the LH component is eventually reflected back as it experiences the local spin-dependent photonic bandgap pertaining to the structure near the exit facet. Such a self polarization filtering appears as a notable added value compared to the nonchiral spin-orbit transmissive counterpart [22], which requires circular polarization filtering in order to extract the optical vortex beam from a composite output field.

Interestingly, the optical diode effect reported here appears as an extension of a previously reported diode effect based on a heterophotonic bandgap structure consisting of an anisotropic nematic layer—which plays the role of a half-wave plate—sandwiched between two cholesteric layers with two different helical pitch values [23]. And this, for three reasons: (i) the polarization conversion takes place in a spatially distributed manner all along the propagation through the medium, (ii) the effective birefringence associated with the umbilic-like helical field varies in space, and (iii) the helical pitch of the chiral structure continuously varies throughout the whole bulk of the medium. Remarkably, from an engineering point of view, such a 3D hybridization between chirality and anisotropy does not require any machining technique, as it results from a self-organization process that would be difficult to achieve otherwise. Noting that similar 3D chiral architectures have been observed in electrically driven cholesteric films [24], the advent of tunable and/or reconfigurable spin-orbit diode effects could be considered. Finally, recalling the well-referenced similarity between the polygonal texture in cholesterics and the structural organization of chitin in living matter such as in insect cuticles [14,25], our findings invite consideration of spin-orbit photonics from a biological perspective.

Funding. Labex NEXT (ANR-11-IDEX- 0002-02); Calmip (P19042); Initiative of Excellence of the University of Bordeaux (ANR-10-IDEX-03-02).

Acknowledgment. We acknowledge the Calmip computing facilities. We thank Chloé Bayon for the TEM image and Grégory Seine for the AFM image.

Disclosures. The authors declare no conflicts of interest.

Data availability. Data underlying the presented results may be obtained from the authors upon reasonable request.

REFERENCES

1. K. Y. Bliokh, F. J. Rodriguez-Fortuno, F. Nori, and A. V. Zayats, Nat. Photonics **9**, 796 (2015).
2. A. Aiello, P. Banzer, M. Neugebauer, and G. Leuchs, Nat. Photonics **9**, 789 (2015).
3. F. Cardano and L. Marrucci, Nat. Photonics **9**, 776 (2015).
4. J. Kim, Y. Li, M. N. Miskiewicz, C. Oh, M. W. Kudenov, and M. J. Escuti, Optica **2**, 958 (2015).
5. P. Chen, B.-Y. Wei, W. Ji, S.-J. Ge, W. Hu, F. Xu, V. Chigrinov, and Y.-Q. Lu, Photon. Res. **3**, 133 (2015).
6. N. Tabirian, H. Xianyu, and E. Serabyn, in *IEEE Aerospace Conference* (2015), pp. 1–10.
7. Y. Li, J. Kim, and M. J. Escuti, Proc. SPIE **8274**, 827415 (2012).
8. E. Serabyn, C. M. Prada, P. Chen, and D. Mawet, J. Opt. Soc. Am. B **36**, D13 (2019).
9. J. Kobashi, H. Yoshida, and M. Ozaki, Nat. Photonics **10**, 389 (2016).
10. M. Rafayelyan, G. Tkachenko, and E. Brasselet, Phys. Rev. Lett. **116**, 253902 (2016).
11. R. Barboza, U. Bortolozzo, M. G. Clerc, and S. Residori, Phys. Rev. Lett. **117**, 053903 (2016).
12. M. Mitov, Adv. Mater. **24**, 6260 (2012).
13. Y. Bouligand, J. Phys. **33**, 715 (1972).
14. G. Agez, C. Bayon, and M. Mitov, Acta Biomater. **48**, 357 (2017).
15. M. Rafayelyan and E. Brasselet, Opt. Lett. **41**, 3972 (2016).
16. J. Kobashi, H. Yoshida, and M. Ozaki, Phys. Rev. Lett. **116**, 253903 (2016).
17. G. Agez, R. Bitar, and M. Mitov, Soft Matter **7**, 2841 (2011).
18. T. J. Bunning, D. L. Vezie, P. F. Lloyd, P. D. Haaland, E. L. Thomas, and W. W. Adams, Liq. Cryst. **16**, 769 (1994).
19. A. Taflove, A. Oskooi, and S. G. Johnson, *Advances in FDTD Computational Electrodynamics: Photonics and Nanotechnology* (Artech House, 2013).
20. A. F. Oskooi, D. Roundy, M. Ibanescu, P. Bermel, J. D. Joannopoulos, and S. G. Johnson, Comput. Phys. Commun. **181**, 687 (2010).
21. G. Friedel, Ann. Phys. **9**, 273 (1922).
22. E. Brasselet and C. Loussert, Opt. Lett. **36**, 719 (2011).
23. J. Hwang, M. H. Song, B. Park, S. Nishimura, T. Toyooka, J. Wu, Y. Takanishi, K. Ishikawa, and H. Takezoe, Nat. Mater. **4**, 383 (2005).
24. B. I. Senyuk, I. I. Smalyukh, and O. D. Lavrentovich, Opt. Lett. **30**, 349 (2005).
25. V. Sharma, M. Crne, J. O. Park, and M. Srinivasarao, Science **325**, 449 (2009).